Special Issue Research Article

NMR IN BIOMEDICINE

Received: 1 April 2010, Revised: 27 May 2010, Accepted: 7 June 2010, Published online in Wiley Online Library: 2010

(wileyonlinelibrary.com) DOI:10.1002/nbm.1591

A system and mathematical framework to model shear flow effects in biomedical DW-imaging and spectroscopy‡

Uri Nevo[a,b], Evren Özarslan[b], Michal E. Komlosh[b], Cheng Guan Koay[b], Joelle E. Sarlls[b] and Peter J. Basser[b]*,†

The pulsed-field gradient (PFG) MR experiment enables one to measure particle displacements, velocities, and even higher moments of complex fluid motions. In diffusion-weighted MRI (DWI) in living tissue, where the PFG MRI experiment is used to measure diffusion, Brownian motion is assumed to dominate the displacements causing the observed signal loss. However, motions of water molecules caused by various active biological processes occurring at different length and time scales may also cause additional dephasing of magnetization and signal loss. To help understand their relative effects on the DWI signal attenuation, we used an integrated experimental and theoretical framework: a Rheo-NMR, which served as an experimental model system to precisely prescribe a microscopic velocity distribution; and a mathematical model that relates the DW signal intensity in the Rheo-NMR to experimental parameters that characterize the impressed velocity field. A technical innovation reported here is our use of 'natural' (in this case, polar) coordinates both to simplify the description the fluid motion within the Couette cell of the Rheo-NMR, as well as to acquire and reconstruct magnitude and phase MR images obtained within it. We use this integrated model system to demonstrate how shear flows appears as pseudo-diffusion in magnitude DW MR signals obtained using PFG spin-echo (PGSE) NMR and MRI sequences. Our results lead us to reinterpret the possible causes of signal loss in DWI *in vivo*, in particular to revise and generalize the previous notion of intra-voxel incoherent motion (IVIM) in order to describe activity driven flows that appear as pseudo-diffusion over multiple length and time scales in living tissues. Published © 2010 John Wiley & Sons, Ltd.

Keywords: DWI, pseudo-diffusion; transport; multiple-scales; IVIM; Rheo-NMR; shear flow; in vivo

INTRODUCTION

NMR is an invaluable tool for characterizing complex molecular motions. In particular, the pulsed-field gradient (PFG) NMR (1) and MRI (2) experiments provide a means to measure particle displacements, velocities, and even higher moments. These measurements are used to glean important features of complex fluid motions from both the phase and magnitude of the measured NMR echo.

In biological and clinical applications of the PFG experiment, the magnitude of the spin echo is used to measure an apparent diffusion coefficient (ADC) (3) or an apparent diffusion tensor (ADT) of water molecules (4,5). It is often presumed that the ADC or ADT results from free or hindered diffusion of water in tissues. A number of studies have hypothesized that other physical processes also contribute to the MR signal loss, including variations in tissue temperature (6,7), changes in intracellular viscosity (8,9), changes in membrane permeability (10,11), and blood flow through randomly oriented capillary networks (12).

Enigmas related to the biophysical basis of the diffusion weighted signal

Despite the widespread uses of diffusion MRI and diffusion tensor MRI (DTI), the biophysical basis of acquired DW signals and their observed changes in development or in pathological conditions, are only partly understood (13). The signal attenuation in a DWI experiment is usually attributed to restricted and/or hindered diffusion that is determined by cell microstructure (14,15). Tissues are usually modeled as static porous media having different intra- and extra-cellular NMR and transport properties (14–17). Yet, to date, it has not been possible to derive the ADC or DTI-related

* *Correspondence to: P. J. Basser, NIH, 13 South Drive, MSC 5772, Building 13, Room 3W16, Bethesda, MD 20892 USA.*
E-mail: pjbasser@helix.nih.gov

a *U. Nevo*
Department of Biomedical Engineering, Tel Aviv University, Ramat Aviv, Tel Aviv 69978, Israel

b *U. Nevo, E. Özarslan, M. E. Komlosh, C. G. Koay, J. E. Sarlls, P. J. Basser*
Section on Tissue Biophysics and Biomimetics (STBB), Eunice Kennedy Shriver National Institute of Child Health and Human Development (NICHD), NIH, Bethesda, MD, USA

‡ *This article is published in NMR in Biomedicine as a special issue on Progress in Diffusion-Weighted Imaging: Concepts, Techniques, and Applications to the Central Nervous System, edited by Jens H. Jensen and Joseph A. Helpern, Center for Biomedical Imaging, Department of Radiology, NYU School of Medicine, New York, NY, USA.*

Abbreviations used: *ADC, apparent diffusion coefficient; ADT, apparent diffusion tensor; cST, centistokes; DTI, diffusion tensor MRI; DWI, diffusion weighted imaging; FA, fractional anisotropy; IVIM, intra-voxel incoherent motion; PDMS, polydimethylsiloxane; PFG, pulsed-field gradient; PGSE, pulsed gradient spin echo; PSF, point spread function*

quantities such as the trace and fractional anisotropy (FA) from static microstructure alone. Beaulieu and Allen demonstrated, for instance, that intracellular organelles and the microtubules hardly restrict water displacement, and that the axonal myelin can only explain about 20% of the observed restriction (11,18). In pathologies like acute stroke the observed drop in the Trace (50–70% of its baseline value) or the concomitant changes in FA (19) cannot be explained by models of restricted diffusion and cell swelling. Moreover, models that describe the apparent multi-exponential decay of the DWI signal attenuation curves, attempting to assign 'fast' and 'slow' components of the DWI to the extracellular and intracellular compartments, respectively, have repeatedly failed to estimate the proper extra- and intracellular volume (16). Sehy *et al.* indeed demonstrated that the intracellular medium includes in it both 'fast' and 'slow' components of displacement (20). The general discrepancies between models of water displacements and DWI experiments prevent the quantitative assessment of tissue microstructure, limit their diagnostic value, and are problematic from a scientific perspective.

The IVIM model

Le Bihan *et al.* (12) first proposed the seminal idea that blood flow in capillaries would also result in signal attenuation in PFG experiments. Specifically, they argued that microcirculation of blood within a random network of capillaries can produce incoherent motions or pseudo-diffusion (which they named intravoxel incoherent motion or IVIM) (12,21). The IVIM concept raised for the first time the possibility that non-diffusive but random convective motions could appear as diffusion within a voxel. Nevertheless, it is important to point out that the IVIM concept has only been applied to capillary blood flow. Capillaries, in this model, are treated as a network of impermeable tubes isolated from the interstitial spaces (12,21). This view requirement caps the maximum relative contribution of the IVIM pseudo-diffusion effect to the relative volume of the capillary bed (3–5% of the tissue volume). Moreover, the length scale for pseudo-diffusion in the IVIM framework is determined by velocities within the capillaries (1–2 mm/s) and the time scale set by the heart rate (about 1 Hz). The result is that the IVIM framework only considers large apparent random displacements, generally as large or larger than the displacements of water caused by free diffusion, that are detectable only at low b-values. Finally, by viewing the intra-capillaries volume, the IVIM refers only to the displacement of blood, which is characterized by a shorter $T2^*$, and is thus less visible in DWI measurements.

A suggested paradigm shift: Multi-scale Pseudo-diffusion

We suggest that in biological systems pseudo-diffusion can occur over a large range of length scales, corresponding to different levels of hierarchical organization (i.e. within organs, tissue extracellular matrix, cells, and across membranes), and over a large range of time scales (i.e. from seconds to microseconds). A unifying feature of these complex motions is that they are all ultimately caused by active energy-consuming biological processes operating at different length and time scales themselves, ranging from respiratory and circulatory system-induced fluid displacements, to dynamic rearrangement of organelles such as the Endoplasmic Reticulum, to the action of membrane pumps like Aquaporin-4. We have named the complex random motions these various processes produce Multi-scale Pseudo-diffusion.

Cellular activity induced displacements

Active processes within cells may produce shear flows and patterns of water mixing. Flow in cells is characterized by very low Reynolds numbers (Re $\sim 10^{-4}$). As a result, it is laminar, and slow displacements can act over long distances (implying that the effect of shear flow may be non-negligible). Absence of significant inertial forces suggests that once the driving forces (e.g. electrostatic forces, drag caused by a moving organelle) stop, flow immediately ceases. Mechanisms of cellular activity that are accompanied by water displacements include but are not limited to: (a) fast and slow axonal transport and water motion induced by dynamic processes within intracellular organelles. For instance, velocities observed in axonal transport are on the order of $\sim$0.5–5 μm/s. This mechanism has the potential of affecting considerable intracellular volume, particularly in brain parenchyma where it has been measured to be about 80% of the total tissue volume (22). (b) Water motion through ion channels and pumps. Ions flowing across membranes are surrounded by a hydration shell. On top of the continuous flow of ions across membranes, a relatively small number of additional ions and water molecules cross membranes during an action potential ($\sim 10^{12}$ molecules/cm^2). The contribution of these water molecules to the overall signal measured in DWI is further reduced by the possible interaction with membranes that may considerably shortens their T2, thus making them invisible in most MRI measurements. (c) Water displacement across Aquaporin channels. As with ion channels the average distances traveled by molecules that are displaced by water channels are assumed to be much less than 1 μm (membrane thickness is of the scale of 10 nm). Nevertheless, exchange of water molecules through Aquaporins is two to three orders of magnitude faster than exchange across a lipid bi-layer, and is supposed to compensate for osmotic flow and diffusion across the bi-layer. We could not find definitive numbers for the rate of exchange of water molecules across the Aquaporin-4 that is expressed in the brain. [Data from a PGSE NMR experiment in red blood cells can give us a clue of the possible relative contribution of Aquaporins to displacement of water molecules. The exchange as a result of lipid permeability and to Aquaporin-1 activity was performed across knock-out mice. Comparison of exchange because of lipid permeability relative to Aquaporin-1 activity resulted in respective relative fractions of 23% and 64% in isotonic conditions, and 10% and $>$ 83% when osmosis took place (23).] (d) Electrical activity – recently suggested to affect the measured displacement, through a phase transition of the water, shifting across ordered and non-ordered lattice, such that their diffusion and relaxation properties are affected (24). (e) Mechanical displacement of the cell membrane. During neuronal activity, the membrane was found to change shape and become displaced (25). (f) Cytoplasmic streaming is a central fluid flow mechanism observed in all cells (and quantified mainly in plant cells). This mechanism affects the entire intracellular volume. And yet it is possible that its physical origin is linked to one of the mechanisms described earlier.

Circulation-induced displacements

As implied above, the capillary bed itself contributes to fluid displacements within the interstitium. Circulation-induced displacement mechanisms that are accompanied by water displacement include: (a) intravascular flow – this is the original IVIM effect that occurs with velocities on the order of 1 mm/s, along capillaries (12). (b) Extravasation of macromolecules and of accompanying water molecules from capillaries – diffusion and convection as a result of hydraulic and osmotic pressure result in displacement across capillaries, resulting in velocities measured to be in the order of 1–10 μm/s (26,27). The amount of fluid that is displaced in this mechanism may be significant, but recent studies have demonstrated that the displacement is governed by diffusion. (c) Pressure pulse waves in capillaries as a result of cardiovascular activity. (d) Quasi-periodic displacements because of the periodic cardiovascular pressure – on the one hand there is a bulk periodic movement of the entire brain that occurs during the cardiac cycle (28). On top of this baseline motion of the entire brain (a coherent motion) it is possible that there are periodic pulses of interstitial fluid displacement that occur as a result of pressure waves during the cardiovascular cycle. It should be noted that the use of cardiac gating in DWI measurements, which has become a standard method, should minimize or even eliminate this effect.

The exact contribution of each of these mechanisms to the measured ADC should be the subject of careful study. Nevertheless, it is already possible to use the 'zeroth-order' knowledge about these mechanisms, in order to understand that pseudo-diffusive displacements that occur by active mechanisms are characterized by multiple length and time scales.

Cessation of activity results in reduced Pseudo-Diffusion

The hypothesis that mechanisms of Multi-Scale Pseudo-Diffusion contribute to the DW signal measured *in vivo* provides a way to address the open questions described above. The common basis for all the mentioned mechanisms is their ultimate dependence on ATP utilization. Once a tissue is challenged by energetic failure a cascade of events is initiated, where some have a causal relation, in which cells slow down and later on gradually cease to operate the energy-consuming processes. For instance, the cessation of oxygenated blood flowing to cells in the brain could potentially explain the precipitous drop in the ADC in stroke (19). A reduction in circulation-induced displacements is eventually followed by a reduction in activity-induced displacements at finer and finer length scales that lead to a drop in the ADC. Energetic failure was in many cases reported to result in a drop in the anisotropy [a most significant drop, among the diffusion eigenvalues is in λ_1, the largest eigenvalue (29)]. Pseudo-diffusion mechanisms that occur within organized tissues will enhance the measured anisotropy (as the shear flow is directional). Cessation of such a flow mechanism may thus contribute to the drop in the anisotropy, in addition to other sources of anisotropy that are modulated by damage to the tissue. An additional enigmatic observation relates to the timing of the drop in the ADC after ischemia: cellular depolarization is the electrical correlate to cellular swelling, and should thus appear before the drop in the ADC if the two phenomena have a causal relation. However, de Crespigny *et al.* observed that a significant component of the drop in the ADC precedes the wave of depolarization occurring in the tissue (30). Cessation of pseudo-diffusion mechanisms may explain this enigma, as in the cascade of events that follow the energetic failure, the cessation of energy consuming mechanical processes within the cells, is the first response to insults, before depolarization occurs. This view could also help explain why multi-compartment diffusion models of brain parenchyma (16) repeatedly fail to predict (instead of measure) the correct extracellular and intracellular volume fractions. In these models, the 'fast' diffusing portion of the signal is assigned to arise from the extracellular volume and the 'slow' component arises from the intracellular one. In our view the conventional rationale for making compartmental assignments is flawed: 'fast' and 'slow' displacements do occur, but both exist in the intra- and extracellular compartments. The magnitude of displacements is not modulated only by spatial arrangement but also by the momentary presence of an active mechanism of displacement (31, unpublished data).

Model system development

In attempting to parse or identify the possible microscopic motions that could contribute to changes in the measured ADC or ADT and, in particular, to assess how physiologically produced micro-flows might contribute to DW signal loss, we sought to develop a theoretical framework and to identify or develop an experimental model system in which a known velocity distribution could be impressed and precisely controlled within an MRI scanner, and with which diffusion weighted MR experiments could readily be performed. For this purpose we used the Rheo-NMR system (32,33). This rheometer was designed to operate within a conventional MR scanner and enables the measurement of molecular displacements under precisely controlled shear flow conditions (32,33). The Rheo-NMR produces a well-defined shear field within a liquid that can be used in NMR spectroscopy to provide invaluable information about molecular dynamics in polymer sciences and hydrodynamics applications (33). However, our use of the Rheo-NMR is not conventional. We use it instead as a model system to understand the effect of known symmetrical shear flow fields on the ADC or the ADT.

The Rheo-NMR can also be used in conjunction with MR microimaging to measure the spatial distribution of different NMR parameters within the rotating fluid. MRI within the Rheo-NMR is usually performed using a vertical slice (selected during the NMR excitation period) that contains the axis of rotation and lies perpendicular to the fluid streamlines. As long as the motion of spin-labeled molecules is perpendicular to the imaging plane, no motion artifacts arise (34). However, it is desirable to obtain axial slices that contain entire closed fluid path lines or streamlines (i.e. slices whose plane is perpendicular to the rotation axis). These are of great interest, particularly in PFG experiments where gradients are applied within this slice plane. The acquisition of such slices could aid in: (a) observing complex flow patterns and motion across streamlines that may change with the rotation angle or position within the rheometer; (b) overcoming low SNR to enable microimaging of the flowing fluid by obtaining thick in-plane slices; (c) acquiring velocity fields with high peak velocities, overcoming a problem encountered when the direction of flow is perpendicular to the slice plane; (d) enabling the imaging of complex flow patterns that involve more than one rotating cylinder, such as the four-roll mill (32); and (e) providing a known and well-defined fluid shear field within each in-plane voxel.

NMR IN BIOMEDICINE

The Rheo-NMR provides an ideal test bed to quantify the effects of shear flow: parallel streamlines across which the flow speed changes. With it, we can study how differences in velocity across a voxel will affect the attenuation in a PFG experiment. To do this, we evaluated this effect using the most simple and symmetric cases, those of linear shear and Couette flow. Appendix 1 details our derivation of the expression for the signal attenuation in a PFG experiment for these two flow fields, when spatially averaged within an imaging voxel. The calculation demonstrates that the attenuation in a q-space experiment for the case of a linear shear (with diffusion weighting gradients applied along the average direction of flow) is

$$E_{flow}(q_x, \Delta) = e^{-2\pi i q_x v_{av} \Delta} \cdot s\,inc\,(\pi q_x \beta\, a \Delta)$$

where β is the linear shear rate, Δ is the diffusion time, and a is the spatial extent of the streamline (transverse to the flow direction). For a Couette flow where there is a circular band of shearing fluid, the corresponding expression is given by:

$$E_{band}(\omega(r), t) = \frac{1}{A}\int_{r_{\text{int}}}^{r_{ext}} J_0(\kappa(\omega(r)))\; r\,dr.\; where\; \kappa(r)$$

$$= 4\pi q_x r \sin\left(\frac{\omega(r)\cdot\Delta}{2}\right).$$

In the above equations J_0 is the 0^{th}-order Bessel function of the first kind, $\omega(r)$ is the radially varying angular velocity, and $A = \pi\cdot(r_{\text{ext}}^2 - r_{\text{int}}^2)$ is the area of the rotating band between the inner and outer radii of the cylindrical shell, r_{int} to r_{ext}, respectively, (see Appendix 1).

A physiological scenario of shear flow will most probably include an ensemble of linear and circular flow patterns that are not synchronized, that occur in multiple length and time scales, and with an isotropic or an anisotropic distribution. The formulations derived above can be used as the basis for a statistical analysis of the attenuation in a physiological scenario.

In the MRI community, MR image slices are most commonly acquired using a Cartesian k-space trajectory, and reconstructed by a two-dimensional Fourier transform. The Cartesian framework is usually used for reconstruction, even when points in k-space are sampled with a non-Cartesian grid (e.g. using radial or spiral k-space trajectories). This reconstruction scheme is cumbersome in the Rheo-NMR because: (a) phase encoding applied in the direction of a the moving fluid will result in motion artifacts (e.g. ghosting); (b) while the signal from each voxel will always represent an average of contributions from multiple streamlines having different velocities, the mapping of cylindrical streamlines into a Cartesian grid introduces a spatially dependant partial-volume artifact (see Fig. 1); and (c) uniform Cartesian k-space samples equally weight the spatial-frequency content of the image. However, in the case of the Rheo-NMR, this needlessly weights high spatial frequencies that are generally produced at liquid-solid interfaces (e.g. fluid-cylinder boundaries in Couette cells) and corners (e.g. near the cone's tip in a cone-and plate viscometer); and (d) the point spread function (PSF) of a polar sampling scheme that includes re-gridding to Cartesian coordinates has significant side-lobes, resulting in aliasing (35). To address these problems, we also developed an MRI acquisition scheme and analytical framework optimized for imaging symmetrical shear flow patterns in their 'natural' coordinates within the Rheo-NMR (see Appendix 2). (Fig. 2)

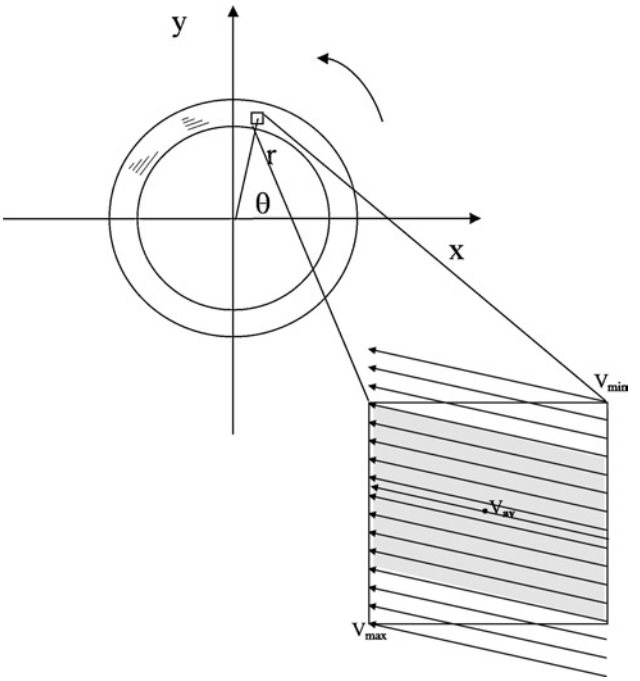

Figure 1. A circular shear flow with an enlarged Cartesian voxel in a Rheo-NMR imaging experiment. Note the partial volume artifact owing to different streamlines flowing through the cubical voxel depending on the direction of flow within each voxel and the voxel's orientation within the laboratory coordinate frame.

METHODS

Acquisition

To test and validate the derived relationships (see Appendices) we used the Bruker Rheo-NMR attachment with a Couette cell (1.7 cm ID, 1.9 cm OD) inside a 7-Tesla vertical-bore MRI scanner (Bruker, Ettlingen, Germany). The gap between the inner and outer cylinders of the Couette cell was filled with a poly-dimethyl-siloxane (PDMS) solution with a viscosity of 1000 cSt and a diffusivity of approximately 4×10^{-6} mm^2/s. The use of this highly viscous and low diffusivity solution allows us to establish a constant shear rate with negligible diffusive or dispersive effects. The inner cylinder of the cell was rotated by a stepper motor at an angular frequency of 1.92 rpm, resulting in a maximal shear rate of 0.294 s^{-1}. Rotation frequency was chosen to obtain a significant shear across single voxels and to illustrate and discriminate the effect of attenuation as a result of shear relative to that which is due to diffusion. The Couette cell was placed within a standard 6-element 30-mm RF coil. Scans were performed at room temperature (20°C).

In the first case, NMR (spectroscopy) scans with varying diffusion gradients were used to mimic a single voxel containing an eddy or closed circulating currents. The spectroscopy PGSE experiments (i.e. with no imaging gradients) were performed with TR/TE = 6000/300 ms, Δ/δ = 200/12 ms, G_d = 0-60 mT/m (65 values). To avoid contamination of the signal from regions at the ends of the coil where the B0 and B1 fields are inhomogeneous, slice selection gradients were used (with slice thicknesses in the range of 0.8–1.2 cm). In the radial PGSE MRI experiments k-space was covered by repeating the experiment in 360 directions and with 512 samples for each line of k-space, using five gradient strengths in the range G_d = 0-40 mT/m. The angles between the

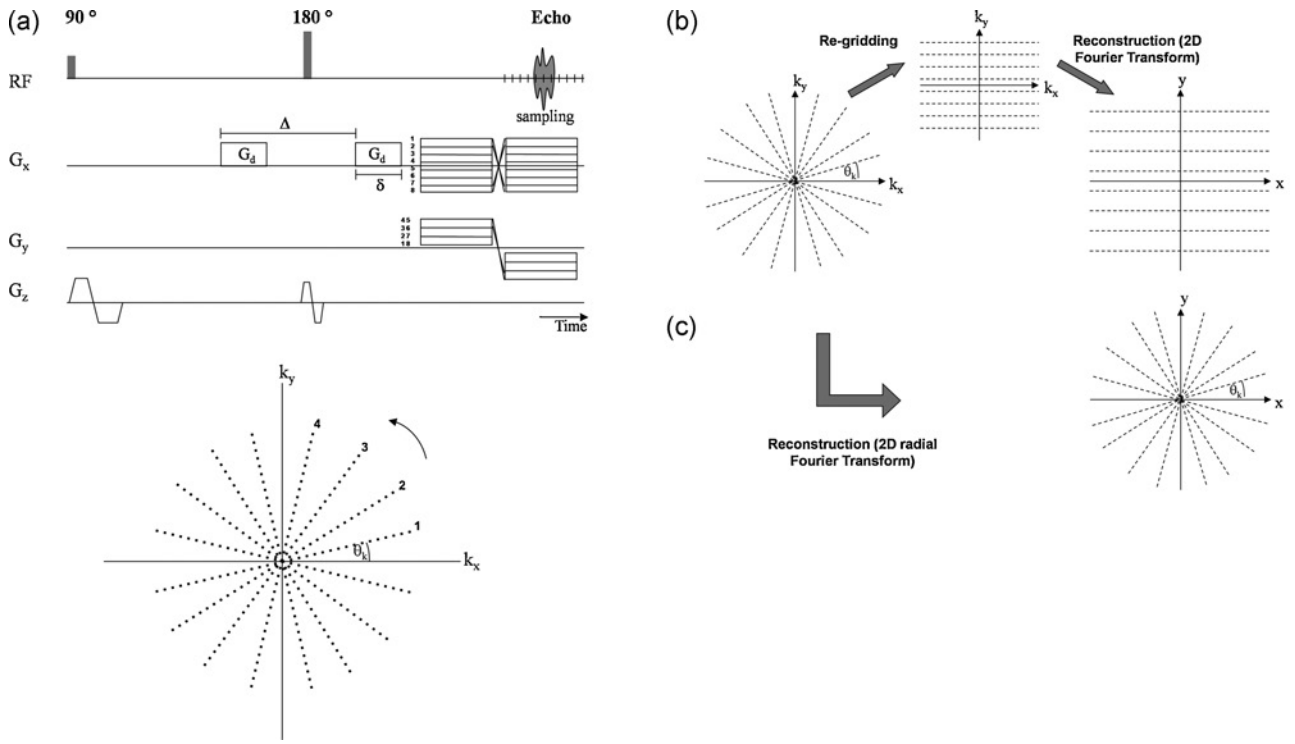

Figure 2. The radial framework: (a) A simplistic radial PGSE pulse sequence, including diffusion gradients in X (G_d), in-plane imaging gradients in X and Y, and slice selection gradients in Z. (b) Common Cartesian reconstruction of radially sampled k-space. (c) The radial reconstruction.

sampled lines in k-space and the x-axis covered the interval $[0,\pi]$, where positive and negative k-values lead to θ_k values covering the entire $[0,2\pi]$ interval. The spatial resolution was $\sim$75 μm along the radial axis, with 0.5° angular or azimuthal increments. Parameters TR/TE/Δ/δ were kept the same as in the NMR spectroscopy experiments. SNR of the reconstructed images was very high (S/N = 25-100).

Image analysis

Magnitude and phase images were reconstructed by employing a Fourier transform in polar coordinates. We calculated both the full Fourier integral (Appendix 2, Eq. 15) and the Bessel expansion of the integral (Appendix 2, Eq. 17). Prior to calculation, the matrix of k-space samples was fitted to polar coordinates such that negative k-space locations with angle θ were treated as positive locations with the angle $180 + \theta$. Data-analysis and simulations were performed using in-house software routines written in Matlab™ and Mathematica™.

RESULTS

NMR of a closed rotating ring (Spectroscopy)

Figure 3 shows the measured signal attenuation in a PGSE experiment for fluid within a rotating Couette cell. Experimental data fits the predictions of our analytical model (given by Eq. 9). Disparities are probably because of strong RF inhomogeneity and possibly additional inhomogeneities in the B0 and B1 fields (as we used a regular 6-elements RF coil and our sample is much larger than the focal center of our scanner). The oscillations of the Bessel function are apparent in the data. In a more heterogeneous flow field these oscillations would be averaged out and not appear. In addition, the attenuation versus the gradient strength is characterized by a sharp drop in slope followed by a region with a moderate slope. The attenuation profile would have the appearance of a bi-exponential that could be inappropriately interpreted as arising from 'fast' and 'slow' diffusing components (Fig. 3). For effect, we performed a two-compartment fit on our data and obtained $D_{fast} = 0.0148$ and $D_{slow} = 0.00037$ mm^2/s (with ratio of fast/slow species being 0.81:019). Notice the curve that displays the attenuation in the absence of shear flow (Fig. 3, green curve) barely drops over the q-values applied, indicating the diffusion coefficient of PDMS in the absence of flow is

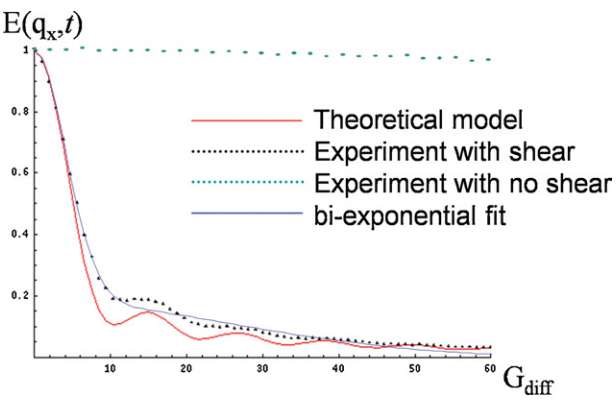

Figure 3. Theoretical and experimental curves for the attenuation caused by shear displacements in a rotating Couette cell during a PGSE-NMR experiment. Experimental curves with and without shear flow appear, respectively, in dotted black and green curves. Theoretical model (with shear), and the fit of a bi-exponential model, appear, respectively, as solid red and blue curves.

3.75×10^{-6} mm^2/s. For clarification, the measured ADC with diffusion weighting along the Z-axis was as that measured in the absence of shear. The differences between the signal attenuations with and without impressed shear flows are significant both qualitatively and quantitatively. The higher the shear-related mixing, the greater the signal attenuation and the greater the departure from mono-exponential decay curves.

MRI within a Couette cell (Imaging)

The acquired k-spaces (magnitudes) for a rotating Couette cell in a PGSE experiment are juxtaposed in Figure 4. The top plot describes the non-weighted acquisition, where the anisotropic pattern (6 'beams') results from RF inhomogeneity (from a 6-element RF coil). Plots at the bottom correspond to the displacement weighted images. Notice the dominance of high spatial frequencies for samples with high k_r values as a result of the strong angle-dependent attenuation. The reconstructed images (magnitude and phase) for the same k-space samples are shown in Figure 5, where reconstructions were performed with the full Fourier transform (Appendix 2, Eq. 15). The top panel presents the reconstructed raw-data and supports our assumption of RF inhomogeneity (that also affected the NMR scan) because of the use of the 6-element RF coil. The pattern of signal attenuation across the Rheo-NMR's Couette cell is as expected from the dephasing of displaced molecules in fluid layers having different average rotational speeds that result in local intra-voxel dephasing. This periodic phase modulation (Fig. 5b) depends on the projection of the average velocity in the direction of the gradient, and thus changes rapidly in the regions where flow is in the direction of the applied diffusion gradient (Fig. 5b). In the magnitude images this velocity field creates an attenuation pattern consisting of two polar regions of the Couette ring with low attenuation (corresponding to regions where flow is perpendicular to the gradient direction) and two polar regions with high attenuation (corresponding to regions where flow is parallel to the gradient direction).

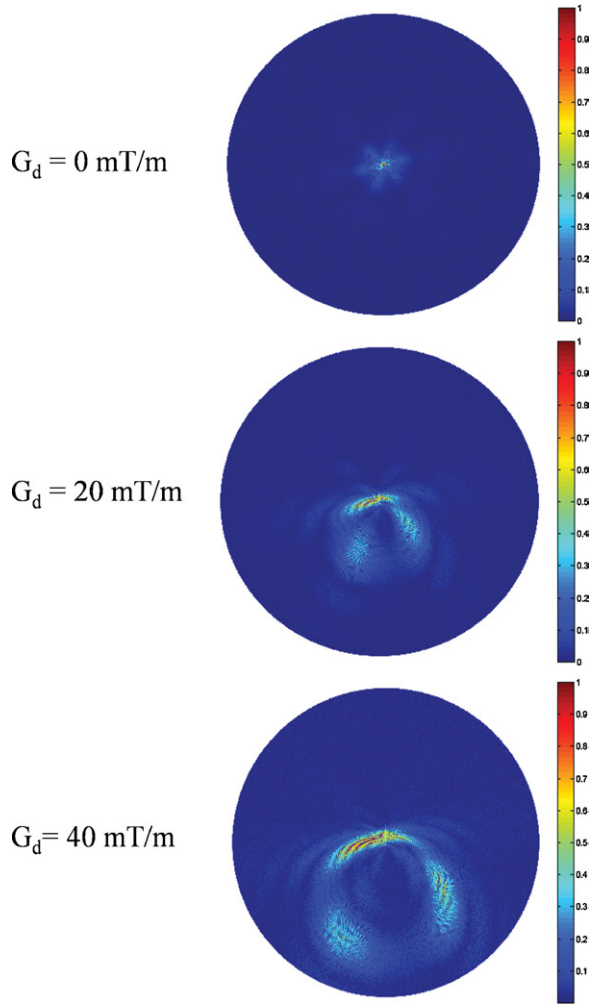

Figure 4. In-plane k-space data resulting from radial sampling in a Rheo-imaging experiment: three plots correspond to MRI with varying values of the diffusion gradient. $G_d = 0$, 20, 40 mT/m. Effective diffusion attenuation in these measurements was b-value = 25.5, 818.4, 3196.9 s/mm^2. Intensities in the first plot are generally higher than in the other plots. However, to allow for a more consistent presentation, the intensities in each were linearly scaled in the range 0–1.

DISCUSSION

A bi-exponential attenuation curve is commonly used in MRI measurements of viable brain tissue (36,37). Moreover, in stroke and other pathological conditions, changes in the relative volume fractions of the two components are often used to infer changes in the relative sizes of these purported compartments, with the partial fraction of the 'slow' component generally increasing at the expense of the size of the 'fast' component (38). Results from fixed tissues clearly indicate that multiple compartments exist in tissues, and that these compartments contribute to a bi-exponential pattern of the attenuation curve. Here we suggest that in addition to this morphological effect, the apparent fast and slow diffusion coefficients and their relative compartment fractions could also be influenced by active flow processes. Such pseudo-diffusion would appear in a PFG measurement as an increase in diffusivity. Some of the observed discrepancies between experiment and theory in biological DW-MRI (39) may possibly be explained by such active flow mechanisms.

The analysis and experiment presented above should help quantify the origin of the signal loss resulting from IVIM, but not just resulting from capillary blood flow. Other sources of IVIM are plasma are plasma exudation in the extracellular spaces, as well as macroscopic motions caused by respiratory cycles, pulse wave propagation of blood, and even slow vasomotion. These could all contribute to complicated water velocity profiles within macroscopic voxels, which appear in the PFG experiment as pseudo-diffusion. Moreover, at smaller, microscopic or cellular length scales, complicated three-dimensional velocity distributions could arise, such as dipolar velocity distributions resulting from the extension or retraction of arrays of microtubules and actin, by cytosolic streaming, or by water pumping across membranes. These could all produce intravoxel MR signal loss, as well.

As noted earlier, multiple biological mechanisms can result in shear flow. An order of magnitude estimate can be made for the DW signal attenuation caused by these physiological mechanisms, even without knowing their precise velocity profiles. Fig. 6 shows the attenuation caused in the simplest case of linear shear for various values of experimental parameters (Δ, q), relative to that of a sample that diffuses freely with an average ADC of

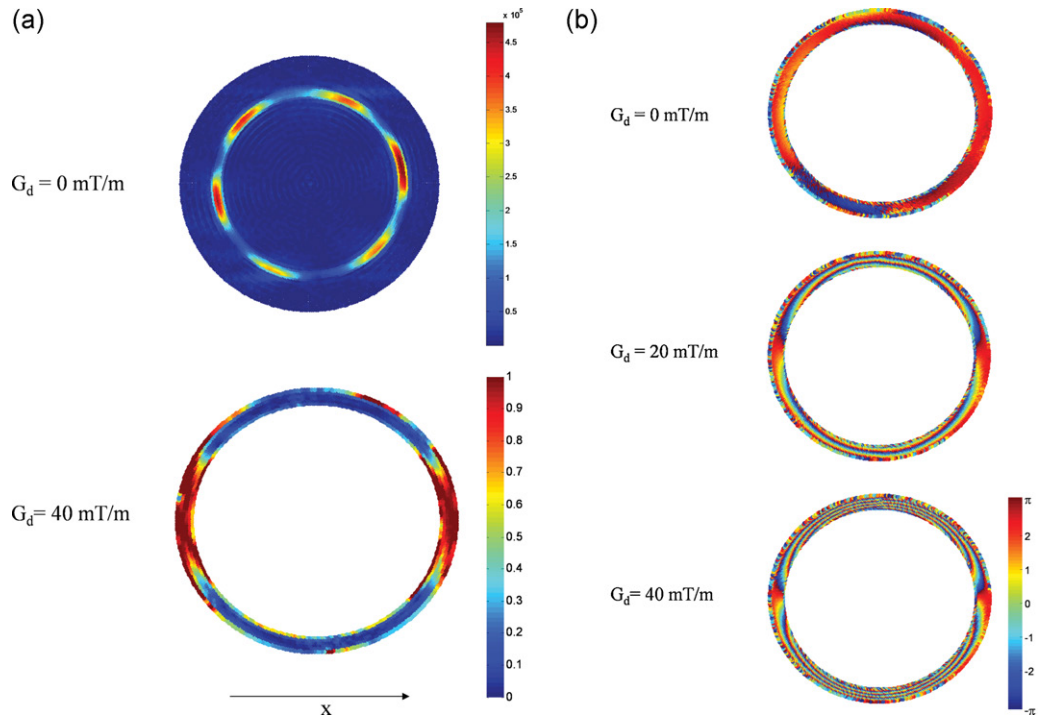

Figure 5. Experimental data and simulation of the net in-plane magnetization in a Rheo-NMR MRI experiment with flow and negligible diffusion. (a) Magnitude images depicting the shear-rate caused attenuation in a PGSE experiment. Arrow marks the x-direction where the diffusion gradient was applied. For didactic purposes, data were under-sampled (by disregarding data points at high k-values) prior to reconstruction, in order to obtain larger voxels (in both *r* and θ coordinates) such that the effect of shear flow would be visible. (b) Phase images depicting the shear-originated phase in a PGSE experiment. To avoid cluttered plots as a result of the random phase in areas with no fluid, these images show only voxels that describe the Couette cell itself.

1×10^{-5} cm^2/s. The regime of commonly used b-values (b< 2000s/mm^2) appears with a dashed outline. Owing to the dearth of measurements of shear rates occurring in neurons, we took the drag of a fluid that may accompany axonal transport as a typical mechanism that may result in shear as an example. Velocities associated with axonal transport (either fast or stop-and-go slow transport) are in the range of ~0.5-5 μm/s (41). In a 1-μm thick axon, such a velocity may cause a maximal linear shear rate of $\beta = 10\,s^{-1}$. This model ignores multiple unknown parameters that affect shear flow: the effect of Actin and microtubules, the viscosity of the complex gel in different length scales, the exact kinetics of the stop-and-go process, etc. Nevertheless, a few quick inferences can be drawn (Fig. 6): (a) with shear rates that are feasible in living tissues, the attenuation induced by the shear field may contribute significantly to that induced by Brownian motion; (b) as expected, the relative contribution of shear-related attenuation increases with longer measurement times (Δ) (a result of the linear increase in displacements as a result of shear flow as compared with the square-root law governing Brownian displacements) and higher q-values; (c) shear flow in an ordered non-isotropic tissue may result in an apparent anisotropic displacement profile, and an anisotropic attenuation in anisotropic tissue that will augment the diffusion anisotropy because of microstructure and morphology alone, for example, that results from restricted diffusion in anisotropic structures.

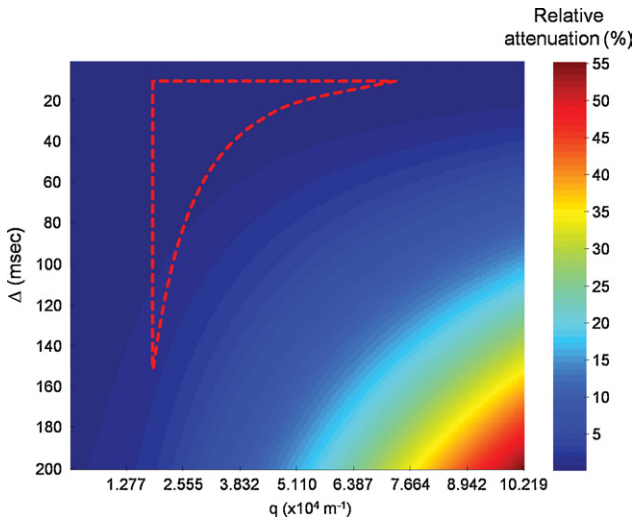

Figure 6. The relative attenuation induced by linear shear for various values of experimental parameters (Δ, q) relative to that of a sample that diffuses freely with an average ADC of $1 \cdot 10^{-5}$ cm^2/s. Colors correspond to the attenuation induced by linear shear, compared with the diffusion-induced attenuation obtained with the same experimental parameters. Dashed lines border the region of commonly used parameters in clinical DWI (b-values < 2000 mm^2/s; Δ= 10–150 ms). Note that the relative contribution of shear-related attenuation increases with longer diffusion times (Δ) and higher q-values.

To apply this new understanding to living tissue quantitatively, we must know the partial volume of intra/extra-cellular fluid that is sheared during the experimental window (Δ), the spatial extent and scales of the shear flow within the imaging voxel, the probability for the occurrence of the shear-inducing mechanism and the relative duration of the mechanical phenomenon linked to it. When the displacement is not entirely dominated by flow, but has a significant component owing to diffusion, and especially when measurement is performed with high q-values, Taylor dispersion may become significant. A first-order approxi-

mation can be obtained by taking only the first displacement cumulant, i.e. assuming that the effect of dispersion is fully described by an adjusted diffusion coefficient. In such a case, Eq. 5 can be revised to give:

$$E_{diff}(\overline{q},\Delta) = e^{-4\pi^2\left(q_x{}^2(1+f_{Taylor})+q_y{}^2+q_z{}^2\right)D\Delta} \quad \text{where} \quad f_{Taylor} = \frac{D^*_{Taylor}-D}{D}.$$

Additional displacement cumulants appear if the geometry restricts the displacement or if high q-values are used (41). In cases where the tissue is not all coherently aligned, powder-averaging may take place. We did not take these factors into account; they should be accounted for separately and evaluated for various physiological conditions. Finally, if shear flow is created by active, energy-consuming mechanisms, any stress on the cells (e.g. hypoxia) may stop the shear-inducing mechanisms and result in reduced signal attenuation and a smaller ADC. Alternatively, any increase in cell activity could result in an increased ADC.

The discrimination of displacements that originate from active cellular mechanisms can be of high value for the study of cellular vitality and function. However, the choice of an experimental and analytical framework is crucial to succeed in this task. DWI is commonly performed using multiple b-values, as well as the more accurate and orientation invariant DTI framework that employs b-matrices. These b-factor based frameworks are inadequate for treating pseudo-diffusion in tissues, however, as they lump together information about the length and time scales of the fluid motion. Specifically, b-values/matrices combine Δ, the diffusion time, and $q = \gamma G_d \delta/(2\pi)$, the quantity that encodes the space scale probed. To follow displacements that occur over multiple length and time scales, the use of the q-space formalism and of advanced q-space MR pulse sequences will be most useful. For example, multi-PGSE pulse sequences (33) used in conjunction with imaging (42) can be used to probe complex motions at different length scales. Different time scales can be probed by varying the diffusion time, Δ, systematically, for instance using a series of standard PGSE experiments with varying Δ, using stimulated-echo DWI to probe long diffusion times (long Δ), or by using oscillating gradient PG approaches (43,44) with different frequencies.

Imaging flow in 'natural coordinates'

The described framework is a particular case of sampling and image reconstruction that is uniquely tailored to exploit the specific symmetry, geometry, and other characteristics of a sample or specimen. An immediate extension of the proposed work is the use of a spherical coordinate system for imaging the fluid in the cone-and-plate rheometer in a Rheo-NMR experiment. Özarslan *et al.* (46) have already described the use of a Fourier transform in spherical coordinates, based on the expansion of the Fourier integrand by spherical harmonics, which could be adapted for this purpose. We tested the effect of voxel sizes and number of radial beams. As expected and predicted by our model, the finer the spatial resolution (i.e. the smaller the voxels, both in the radial and azimuthal dimensions), the smaller the resulting signal attenuation, as the variance in streamline velocities within each voxel is reduced.

The suggested framework may be valuable when complicated flow patterns are involved, as when, for example, MR imaging is combined with pulse sequences that can distinguish between diffusion and velocity-driven mixing. In the case of imaging non-regular patterns (such as shear banding or turbulence), the acquisition method described above may be too slow relative to the time-scales in which these patterns form, or disappear. In that case, as shown by Sarlls *et al.* (46), imaging can be accelerated by the acquisition of multi-echoes. Acquisition speed will then be limited by the decay times (T_2, and to a lesser extent, T_1) and may demand a segmented sampling of k-space.

CONCLUSIONS

The present study provides a new perspective to the problem of identifying sources of displacement of water molecules as measured in DWI. Most models of displacement of water molecules in brain parenchyma treat it as a 'dead' or fixed tissue, in which displacements governed by thermal diffusion, without any contribution of displacements because of active cellular processes. The familiar IVIM concept should also be revisited in light of this study as despite its manifold strengths it considers only pseudo-diffusion arising from capillary blood flow over large length and time scales, and it uses the b-value formalism to characterize pseudo-diffusion experimentally and mathematically. To characterize the relative effects of random Brownian motion and pseudo-diffusion within a voxel, we described a theoretical framework for the analysis of a simple pattern of shear flow. To validate and demonstrate this framework experimentally we developed an acquisition, reconstruction, and analysis framework for diffusion weighted MRI (DWI) data obtained in a controlled system with known shear flows. This experimental framework can be used to estimate the effects that complex flow patterns have on the ADC in living tissue. This work should aid in helping to uncover biophysical mechanisms affecting DWI data in clinical and biological applications.

Acknowledgements

This work was supported by the Intramural Research Program of the Eunice Kennedy Shriver National Institute of Child Health and Human Development, NIH. Uri Nevo is a Colton Foundation Fellow, and is supported by the IRG grant of the EU. We wish to thank Liz Salak for editing this manuscript.

REFERENCES

1. Stejskal EO, Tanner JE. Spin diffusion measurements: Spin echoes in presence of a time-dependent field gradient. J Chem Phys 1965; 42: 288–292.
2. Cory DG, Garroway AN. Measurement of translational displacement probabilities by NMR: an indicator of compartmentation. Magn Reson Med 1990; 14: 435–444.
3. Tanner JE. Self diffusion of water in frog muscle. Biophys J 1979; 28: 107–116.
4. Basser PJ, Mattiello J, Le Bihan D. Estimation of the effective self-diffusion tensor from the NMR Spin-Echo. J Magn Reson B 1994; 103: 247–254.
5. Basser PJ, Mattiello J, Le Bihan D. NMR diffusion tensor spectroscopy and imaging. Biophys J 1994; 66: 259–267.
6. Karaszewski B, Wardlaw JM, Marshall I, Cvoro V, Wartolowska K, Haga K, Armitage PA, Bastin ME, Dennis MS. Measurement of brain temperature with magnetic resonance spectroscopy in acute ischemic stroke. Ann Neurol 2006; 60: 438–446.

7. Marshall I, Karaszewski B, Wardlaw JM, Cvoro V, Wartolowska K, Armitage PA, Carpenter T, Bastin ME, Farrall A, Haga K. Measurement of regional brain temperature using proton spectroscopic imaging: validation and application to acute ischemic stroke. Magn Reson Imaging 2006; 24: 699–706.
8. Minsky A. Structural aspects of DNA repair: the role of restricted diffusion. Mol Microbiol 2003; 50: 367–376.
9. Wolf SG, Frenkiel D, Arad T, Finkel SE, Kolter R, Minsky A. DNA protection by stress-induced biocrystallization. Nature 1999; 400: 83–85.
10. Beaulieu C. The basis of anisotropic water diffusion in the nervous system - a technical review. NMR Biomed 2002; 15: 435–455.
11. Beaulieu C, Allen PS. Water diffusion in the giant axon of the squid: implications for diffusion-weighted MRI of the nervous system. Magn Reson Med 1994; 32: 579–583.
12. Le Bihan D, Breton E, Lallemand D, Grenier P, Cabanis E, Laval-Jeantet M. MR imaging of intravoxel incoherent motions: application to diffusion and perfusion in neurologic disorders. Radiology 1986; 161: 401–407.
13. Norris DG. The effects of microscopic tissue parameters on the diffusion weighted magnetic resonance imaging experiment. NMR Biomed 2001; 14: 77–93.
14. Assaf Y, Blumenfeld-Katzir T, Yovel Y, Basser PJ. AxCaliber: a method for measuring axon diameter distribution from diffusion MRI. Magn Reson Med 2008; 59: 1347–1354.
15. Sen PN, Basser PJ. A model for diffusion in white matter in the brain. Biophys J 2005; 89: 2927–2938.
16. Stanisz GJ, Szafer A, Wright GA, Henkelman RM. An analytical model of restricted diffusion in bovine optic nerve. Magn Reson Med 1997; 37: 103–111.
17. Ozarslan E, Basser PJ, Shepherd TM, Thelwall PE, Vemuri BC, Blackband SJ. Characterization of anomalous diffusion from mr signal may be a new probe to tissue microstructure. Conf Proc IEEE Eng Med Biol Soc 2006; 1: 2256–2259.
18. Beaulieu C, Allen PS. Determinants of anisotropic water diffusion in nerves. Magn Reson Med 1994; 31: 394–400.
19. Beaulieu C, de Crespigny A, Tong DC, Moseley ME, Albers GW, Marks MP. Longitudinal magnetic resonance imaging study of perfusion and diffusion in stroke: evolution of lesion volume and correlation with clinical outcome. Ann Neurol 1999; 46: 568–578.
20. Sehy JV, Ackerman JJ, Neil JJ. Evidence that both fast and slow water ADC components arise from intracellular space. Magn Reson Med 2002; 48: 765–770.
21. Le Bihan D. Intravoxel incoherent motion perfusion MR imaging: a wake-up call. Radiology 2008; 249: 748–752.
22. Krizaj D, Rice ME, Wardle RA, Nicholson C. Water compartmentalization and extracellular tortuosity after osmotic changes in cerebellum of Trachemys scripta. J Physiol 1996; 492(Pt 3): 887–896.
23. Mathai JC, Mori S, Smith BL, Preston GM, Mohandas N, Collins M, van Zijl PC, Zeidel ML, Agre P. Functional analysis of aquaporin-1 deficient red cells. The Colton-null phenotype. J Biol Chem 1996; 271: 1309–1313.
24. Le Bihan D. The 'wet mind': water and functional neuroimaging. Phys Med Biol 2007; 52: R57–90.
25. Tasaki I, Byrne PM. Optical changes during nerve excitation: interpretation on the basis of rapid structural changes in the superficial gel layer of nerve fibers. Physiol Chem Phys Med NMR 1994; 26: 101–110.
26. Chary SR, Jain RK. Direct measurement of interstitial convection and diffusion of albumin in normal and neoplastic tissues by fluorescence photobleaching. Proc Natl Acad Sci U S A 1989; 86: 5385–5389.
27. Jain RK. Transport of molecules, particles, and cells in solid tumors. Annu Rev Biomed Eng 1999; 1: 241–263.
28. Loth F, Yardimci MA, Alperin N. Hydrodynamic modeling of cerebrospinal fluid motion within the spinal cavity. J Biomech Eng 2001; 123: 71–79.
29. Sotak CH. The role of diffusion tensor imaging in the evaluation of ischemic brain injury - a review. NMR Biomed 2002; 15: 561–569.
30. de Crespigny AJ, Rother J, Beaulieu C, Moseley ME, Hoehn M. Rapid monitoring of diffusion, DC potential, and blood oxygenation changes during global ischemia. Effects of hypoglycemia, hyperglycemia, and TTX. Stroke 1999; 30: 2212–2222.
31. Nevo U, Komlosh M, Özarslan E, Basser PJ. Modeling the effect of micro-streaming on DWI data. *SNDS Bi-national Workshop on MRI of Brain Connectivity and Microstructure: Measurement and Validation*. Dead Sea, Israel, 2007.
32. Britton MM, Callaghan PT, Kilfoil ML, Mair RW, Owens KM. NMR velocimetry and spectroscopy at microscopic resolution in small rheometric devices. Appl Magn Reson 1998; 15: 287–301.
33. Callaghan PT. Rheo-NMR: nuclear magnetic resonance and the rheology of complex fluids. Rep Prog Phys 1999; 62: 599–670.
34. Xia Y, Callaghan PT, Jeffrey KR. Imaging Velocity Profiles - Flow through an Abrupt Contraction and Expansion. AIChE J 1992; 38: 1408–1420.
35. Lauzon ML, Rutt BK. Effects of polar sampling in k-space. Magn Reson Med 1996; 36: 940–949.
36. Assaf Y, Cohen Y. In vivo and in vitro bi-exponential diffusion of N-acetyl aspartate (NAA) in rat brain: a potential structural probe? NMR Biomed 1998; 11: 67–74.
37. Mulkern RV, Gudbjartsson H, Westin CF, Zengingonul HP, Gartner W, Guttmann CR, Robertson RL, Kyriakos W, Schwartz R, Holtzman D, Jolesz FA, Maier SE. Multi-component apparent diffusion coefficients in human brain. NMR Biomed 1999; 12: 51–62.
38. Brugieres P, Thomas P, Maraval A, Hosseini H, Combes C, Chafiq A, Ruel L, Breil S, Peschanski M, Gaston A. Water diffusion compartmentation at high b values in ischemic human brain. AJNR Am J Neuroradiol 2004; 25: 692–698.
39. Cohen Y, Assaf Y. High b-value q-space analyzed diffusion-weighted MRS and MRI in neuronal tissues - a technical review. NMR Biomed 2002; 15: 516–542.
40. Brown A. Slow axonal transport: stop and go traffic in the axon. Nat Rev Mol Cell Biol 2000; 1: 153–156.
41. Brenner H, Edwards DA. *Macrotransport Processes*. Butterworth-Heinemann: Boston, 1993.
42. Komlosh ME, Lizak MJ, Horkay F, Freidlin RZ, Basser PJ. Observation of microscopic diffusion anisotropy in the spinal cord using double-pulsed gradient spin echo MRI. Magn Reson Med 2008; 59: 803–809.
43. Schachter M, Does MD, Anderson AW, Gore JC. Measurements of restricted diffusion using an oscillating gradient spin-echo sequence. J Magn Reson 2000; 147: 232–237.
44. Stepisnik J, Callaghan PT. Low-frequency velocity correlation spectrum of fluid in a porous media by modulated gradient spin echo. Magn Reson Imaging 2001; 19: 469–472.
45. Ozarslan E, Shepherd TM, Vemuri BC, Blackband SJ, Mareci TH. Resolution of complex tissue microarchitecture using the diffusion orientation transform (DOT). Neuroimage 2006; 31: 1086–1103.
46. Sarlls JE, Pierpaoli C. Diffusion-weighted radial fast spin-echo for high-resolution diffusion tensor imaging at 3T. Magn Reson Med 2008; 60: 270–276.
47. Hunter MW, Callaghan PT. NMR measurement of nonlocal dispersion in complex flows. Phys Rev Lett 2007; 99: 210602.
48. Guo H, Song AW. *MRI Image Reconstruction by Polar Fourier Transform*. Kyoto, Japan, 2004; 350.

Appendix 1 Quantification of the effect of shear flow on the diffusion weighted signal

To demonstrate the effect of a symmetric shear flow on a DW signal, we use the *q*-space formalism. In a PFG NMR experiment diffusion weighting can be quantified by the wave vector, *q*,

$$q = \frac{\gamma \delta g}{2\pi} \tag{1}$$

with g, the applied diffusion gradient; δ, the duration of the applied gradient pulse; and γ, the gyromagnetic ratio of the detected nuclear spins.

In the PFG NMR experiment, there is an elegant and useful Fourier relationship between the MR signal attenuation, *E(q,t),* and the ensemble average of displacements. These displacements are given by $P_s(R,t)$ that describes the probability for a spin-bearing molecule to be displaced by R, during time t(1).

$$E(q,t) = \int P_s(R,t) e^{i2\pi qR} dR \tag{2}$$

In a scenario where only Brownian motion is present, the resulting probability density is described by a Gaussian.

Linear shear flow

Consider a three-dimensional volume where fluid flows with a uniform linear shear rate, $\beta = \partial Vx/\partial y$, in the x-direction. We will neglect the role of Taylor dispersion (42) by restricting our derivation to the case of fluids with high viscosity or when low q-values are applied in the NMR experiment. In such a case, as the shear–flow and the diffusion are not interacting, the attenuation in a PFG experiment in a square pixel of area a^2, with diffusion time Δ over such a sample will be:

$$E(\overline{q},\Delta) = E_{flow}(q_x,\Delta)\cdot E_{diff}(\overline{q},\Delta) \tag{3}$$

where

$$E_{flow}(q_x,\Delta) = e^{-2\pi i q_x v_{av}\Delta}\cdot s\,inc\,(\pi q_x \beta\, a\Delta) \tag{4}$$

and

$$E_{diff}(\overline{q},\Delta) = e^{-4\pi^2\left({q_x}^2+{q_y}^2+{q_z}^2\right)D\Delta} \quad \text{with} \quad \overline{q} = (q_x, q_y, q_z), \tag{5}$$

where v_{av} is the average velocity within the pixel. In a common DWI experiment, in the absence of analysis that will discriminate shear flow from diffusion, the shear flow causes the ADC to be larger relative to the true self-diffusion coefficient, D. It should be noted that in most works that involve shear flow with a highly viscous fluid (as the one reported here) the effect of Taylor dispersion is assumed to be relatively low (48).

Cylindrical flow

In the case of an axi-symmetric cylindrical flow (Fig. 1) we consider only the E_{flow} term within the Couette cell corresponding to the case where displacements as a result of shear flow dominate (i.e. in the high viscosity or high shear rate regimes). Consider a ring of radius r and an infinitesimal thickness dr, filled with a fluid that rotates at a uniform angular velocity, $\omega(r)$. As each element of that ring is displaced circumferentially, the change in phase it experiences for a diffusion gradient applied along the x axis, is characterized by q_x, and for a diffusion time, Δ, is

$$\Delta\phi = 2\pi q_x r(\cos(\theta+\omega\cdot\Delta)-\cos\theta). \tag{6}$$

Assuming a uniform spin density, the signal attenuation within that ring obtained by integrating over the circle of radius r is:

$$E_{ring}(\omega(r),\Delta) = \frac{1}{2\pi}\int_0^{2\pi} e^{2\pi\, i\, q_x r(\cos(\theta+\omega\cdot\Delta)-\cos\theta)}d\theta$$

$$= \frac{1}{2\pi}\int_0^{2\pi} e^{i\kappa\cdot r\sin\theta}d\theta = J_0(\kappa) \tag{7}$$

$$\kappa(r) = 4\pi q_x r\sin\left(\frac{\omega(r)\cdot\Delta}{2}\right) \tag{8}$$

and J_0 is the 0^{th}-order Bessel function of the first kind. The signal attenuation of a circulating band of fluid of area, $A = \pi\cdot(r_{ext}^2 - r_{int}^2)$ is obtained by integrating over all such rings from r_{int} to r_{ext}, and is thus given by:

$$E_{band}(\omega(r),t) = \frac{1}{A}\int_{r_{int}}^{r_{ext}} J_0(\kappa(\omega(r)))\, r\, dr. \tag{9}$$

This expression describes the attenuation owing to displacements of spin-bearing molecules along closed circular streamlines, as in a Couette cell, where

$$\omega(r) = \frac{\omega_{\max} r_{int}}{r_{ext}^2 - r_{int}^2}\left(\frac{r_{ext}^2}{r} - r\right). \tag{10}$$

Alternatively, this expression could describe the contribution of a single micro-circulatory eddy in an imaging experiment where the voxel's typical size, a, obeys $r << a$.

Appendix 2 Image reconstruction in 'natural' polar coordinates

In the case where a voxel includes only a portion of the circular streamline, we can assign a magnetization density, $M(r,\theta)$, to each element of the rotating ring

$$M(r,\theta) = M_0 e^{i4\pi q_x r\left(\sin\left(\frac{\omega(r)\cdot\Delta}{2}\right)\sin\theta'\right)}, \tag{11}$$

where the angle θ' corrects for the delay between the displacement-encoding period (taken as the midpoint of the displacement encoding period) and the actual acquisition point that occurs during the refocusing of the echo. This delay results in an angular shift:

$$\theta' = \theta - \omega\left(\frac{\Delta}{2} + t_{TE-diff}\right) \tag{12}$$

where $t_{TE\text{-}diff}$ is the delay between the end of the displacement encoding (the application of the second gradient) and the acquisition.

In an MRI experiment where the streamlines are macroscopic (e.g. in a Rheo-NMR experiment), or when imaging is performed with microscopic resolution (i.e. $a \le r\cdot\omega\tau$, where a is the pixel size, r is the distance of the segment from the origin, and $\omega\tau$ is the angle subtended during the time from encoding to detection) each streamline is separated into segments/voxels. A natural and preferred way to acquire MRI data is to use streamlines as voxel boundaries.

A case in point is a Couette cell, where image acquisition and analysis are most elegantly and compactly described in polar coordinates. To exploit the axial symmetry of flow in a Couette cell, we chose cylindrical k-space sampling and reconstruction schemes. MRI acquisition with radial coverage of k-space is used to avoid various imaging artifacts, particularly motion-induced ghosts. In this scheme, in-plane gradients are applied during the sampling of the magnetization $M(k_r,\theta_k)$ (Fig. 2a), where the radial angle of each consecutive line is varied. Usually, axially sampled k-space is re-gridded to Cartesian coordinates for further reconstruction and analysis (Fig. 2b). However, to exploit fully the axial symmetry of the flow in a Couette cell, we performed the entire reconstruction and analysis procedures in polar coordinates as well (Fig. 2c). Lauzon and Rutt (35) showed that the PSF of polar sampling (without re-gridding to Cartesian coordinates) is more centered and includes negligible side lobes relative to the alternative that includes re-gridding.

In Cartesian coordinates, the sampled magnetization $M(k_x,k_y)$ that comprises a plane in k-space, is related to the

local magnetization $M(x,y)$ by the Fourier transform relation:

$$\tilde{M}(k_x,k_y) = \int_{-\infty}^{\infty} dx \int_{-\infty}^{\infty} dy\, M(x,y)\, e^{-i2\pi(k_x x + k_y y)}. \quad (13)$$

The same relation in polar coordinates can be obtained by a familiar change of variables:

$$\tilde{M}(k_r,\theta_k) = \int_0^{\infty} dr\, r \int_0^{2\pi} d\theta_r\, M(r,\theta_r)\, e^{-i\,2\pi k_r r\cos(\theta_r-\theta_k)} \quad (14)$$

where $\tilde{M}(k_r,\theta_k)$ is the radially sampled k-space signal, $M(r,\theta_r)$ is the local magnetization in the 'image' space and $k_r = 2\pi/r$. θ_k andθ_r represent the angles of k-lines or r-lines, in k-space or in r-space, respectively. We are interested in reconstructing the spatial distribution of the magnetization, using the acquired k-space signals.

$$M(r,\theta_r) = \int_0^{\infty} dk\, k \int_0^{2\pi} d\theta_k\, \tilde{M}(k,\theta_k)\, e^{j\,2\pi kr\cos(\theta_r-\theta_k)}. \quad (15)$$

To obtain an expression for the inverse transform, we expand the exponential factor above

$$e^{j\,2\pi\bar{k}\cdot\bar{r}} = \sum_{m=-\infty}^{\infty} i^m J_m(2\pi kr)\, e^{im(\theta_r-\theta_k)} \quad (16)$$

where $J_m(x)$is the m^{th}-order Bessel function. Inserting this expansion for $e^{j\,2\pi\bar{k}\cdot\bar{r}}$ into the formula for the inverse Fourier transform above results in the following expression for $M(r,\theta_r)$ that is straightforward to calculate:

$$M(r,\theta_r) = \sum_{m=-\infty}^{\infty} i^m e^{im\theta_r} \int_0^{\infty} dk_r\, k_r\, J_m(2\pi k_r r) \int_0^{2\pi} d\theta_k\, \tilde{M}(k_r,\theta_k)\, e^{-im\theta_k}. \quad (17)$$

Radial sampling provides a means to obtain planar images with no motion artifacts and to sample spatial frequencies with cylindrical symmetry. In addition, with no additional transforms, a simple natural coordinate system is provided for additional data presentation and analysis. The computation of the expanded Bessel transform is not time consuming. However, Guo and Song (49), who reported a similar approach for MRI, suggested further simplifying using a lookup table to evaluate the Bessel function values.

With this framework, magnetization at each point specified by the polar coordinates (r, θ_r) can be approximated directly from radial k-space data. A comparison of a Rheo-NMR experiment to theory is thus simplified, such that the detected signal intensity I, within a voxel is calculated by:

$$I_{r_1,\phi_1}(\Delta r,\Delta\theta) = \int_{\Delta\theta}\int_{\Delta r} M(r,\theta)\, r\, dr\, d\theta. \quad (18)$$

To reconstruct the magnetization density, we suggest using spatial encoding that exploits the symmetry of the displacement field.